Electroluminescence and Plasmon-Assisted Directional Photoluminescence from 2D HgTe Nanoplatelets

Corentin Dabard, Erwan Bossavit, Tung Huu Dang, Nicolas Ledos, Mariarosa Cavallo, Adrien Khalili, Huichen Zhang, Rodolphe Alchaar, Gilles Patriarche, Angela Vasanelli, et al.

▶ To cite this version:

Corentin Dabard, Erwan Bossavit, Tung Huu Dang, Nicolas Ledos, Mariarosa Cavallo, et al.. Electroluminescence and Plasmon-Assisted Directional Photoluminescence from 2D HgTe Nanoplatelets. Journal of Physical Chemistry C, In press, 10.1021/acs.jpcc.3c04126 . hal-04171375

HAL Id: hal-04171375
https://hal.science/hal-04171375v1

Submitted on 26 Jul 2023

Electroluminescence and Plasmon-Assisted Directional Photoluminescence from 2D HgTe Nanoplatelets

Corentin Dabard[1], Erwan Bossavit[2,3], Tung Huu Dang[2,4], Nicolas Ledos[2], Mariarosa Cavallo[2], Adrien Khalili[2], Huichen Zhang[2], Rodolphe Alchaar[2], Gilles Patriarche[5], Angela Vasanelli[4], Benjamin T. Diroll[6], Aloyse Degiron[7], Emmanuel Lhuillier[2], Sandrine Ithurria[1*]

[1] Laboratoire de Physique et d'Etude des Matériaux, ESPCI-Paris, PSL Research University, Sorbonne Université Univ Paris 06, CNRS UMR 8213, 10 rue Vauquelin 75005 Paris, France.
[2] Sorbonne Université, CNRS, Institut des NanoSciences de Paris, INSP, F-75005 Paris, France.
[3] Synchrotron SOLEIL, L'Orme des Merisiers, Départementale 128, 91190 Saint-Aubin, France.
[4] Laboratoire de physique de l'Ecole Normale Supérieure, ENS, Université PSL, CNRS, Sorbonne Université, Université Paris Cité, 75005 Paris, France
[5] Centre de Nanosciences et de Nanotechnologies, CNRS, Université Paris-Saclay, C2N, Palaiseau 2110, France.
[6] Center for Nanoscale Materials, Argonne National Laboratory, 9700 S. Cass Avenue, Lemont, Illinois 60439, United States
[7] Université Paris Cité, CNRS, Laboratoire Matériaux et Phénomènes Quantiques, 75013 Paris, France.

Abstract: In the visible range, 2D nanoplatelets have brought significant benefits compared to their 0D counterpart with an inherently anisotropic emission, a narrower PL signal and new degrees of freedom to design heterostructures. Compared to the properties of cadmium chalcogenide nanoplatelets in the visible, similar research is still mostly lacking in the infrared, in spite of existing synthetic paths to obtain narrow band gap semiconductors under 2D colloidal form. Here, we focus on 2D HgTe nanoplatelets and show how their photoluminescence can be stabilized through the proper choice of surface chemistry. We then demonstrate two important steps toward bright infrared LEDs which are (*i*) the coupling to a plasmonic grating to control the magnitude and spatial direction of the PL signal and (*ii*) the observation of electroluminescence at 1300 nm, which is near telecom wavelength.

TOC graphic

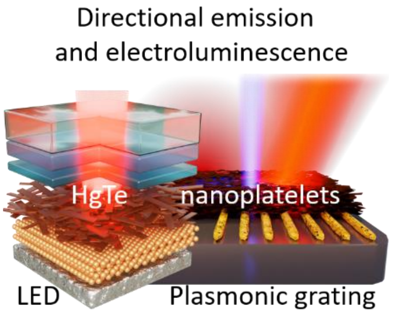

Keywords: HgTe, nanoplatelets, photoluminescence, infrared, LED, plasmon.

*To whom correspondence should be sent: sandrine.ithurria@espci.fr

The introduction of quantum confinement in semiconductor materials enables a continuous tuning of their optical features. This property, combined with bright emission has generated a lot of interest and has led to their first mass market application as light down-converters for displays.[1,2] Here, the spectral linewidth of the emission appears as a critical parameter. In nanocrystal (NC) populations, the narrowness of the luminescence signal is first driven by the particle size distribution (*i.e.* inhomogeneous broadening). This is in turn strongly related to the growth mechanism of the particles and the consecutive selective precipitation process used to sort the particles according to their size. Among the broad family of NCs, 2D nanoplatelets[3] (NPLs) present the narrowest photoluminescence (PL) signal. Actually, this property is not much related to the particle dimensionality, but rather to the specific growth mechanism that enables atomic precision along the NPL thickness. Beyond their spectral linewidth, anisotropically shaped particles also raise interest to achieve macroscopically polarized and directional emission. The latter point appears critical for the integration of NCs in light emitting diodes (LEDs). Random orientation of the emitter combined with the optical index mismatch between air and the emitting medium leads to most (≈80 %) of the emitted photons are not propagating toward the far-field but rather being guided in the substrate. This generates optical losses and Joule heating which further degrades performances. With cadmium-based NPLs, attempts to achieve macroscopic optical properties[4–9] from NPL films have been driven by self-assembly approaches, where the careful tuning of the film preparation enables control of the NPLs' orientation, which allows the film to benefit from the polarization arising from the particle shape.[10–12] However, when it comes to infrared wavelengths, far less work has been devoted to macroscopic optical properties and device integration lags even further behind.[13]

Infrared 2D colloidal materials are driven by narrow band gap semiconductors such as lead[14–16] and mercury[17–20] chalcogenides. These two classes of materials have very different growth mechanisms. In the case of PbS, the growth of the 2D particles results from the oriented attachment of small pre-formed nanocrystals[21]. For mercury chalcogenides[22], no direct growth process of 2D NPLs has been reported. Their synthesis currently requires a two-step procedure: first cadmium chalcogenides NPLs are grown and then a cation exchange[23,24] is performed to replace the native Cd^{2+} ions with Hg^{2+}. For HgTe, when this procedure is conducted slowly enough, the 2D shape of the native CdTe NPLs is preserved. Moreover since the selection rules are the same[24], the absorption spectra are similar but redshifted, with an HgTe NPLs band edge located around 900 nm compared to 500 nm for CdTe NPLs. Tenney *et al*[25] further established that the photoluminescence (PL) spectrum quickly evolves from a band edge driven emission for fresh samples to a lower energy state as the sample aged, due to either the continued growth of small HgTe quantum dots or an imperfect surface passivation.

Here, we investigate the mechanism at the origin of this spectral shift and propose a strategy to stabilize the emission from HgTe NPLs over time which further enables their integration into devices. We then developed a strategy to achieve macroscopically directional emission through the coupling of the HgTe NPLs film to a metallic plasmonic grating. In this case, the directional emission arises from the plasmon dispersion rather than the properties of the individual NPL. Finally, we also demonstrate the integration of such NPLs as the emitting material for near infrared LEDs.

To obtain HgTe NPLs, we start by growing CdTe NPLs. Since PL is the targeted property, we focus here on NPLs with rather small lateral extensions, see Figure S1. Smaller NPLs are less likely to include defects and also have a better colloidal stability, which is a critical property for their following integration in devices with vertical geometry such as diode stacks. The CdTe NPLs are grown using a protocol adapted from Anand *et al*[26]. They are made of 3 monolayers of CdTe (3 layers of tellurium sandwiched between 4 layers of cadmium) and present a first excitonic peak at 500 nm, giving a yellowish color to the solution. We then expose the CdTe NPLs to an Hg precursor enabling a full cation exchange.[23,24] By doing so, the absorption is strongly redshifted and now presents a first absorption peak at 836 nm, see **Figure 1**a. This value is blue shifted in comparison to previous works most probably due to the lateral quantum confinement that appears in small lateral extension NPLs. Indeed, transmission electron microscopy (TEM, see **Figure 1**b) reveals the 2D shape of NPLs and at least one dimension smaller than material Bohr radius (40 nm for HgTe). The absorption spectrum presents a tail below the band edge energy that we attribute to scattering from large scale aggregates.

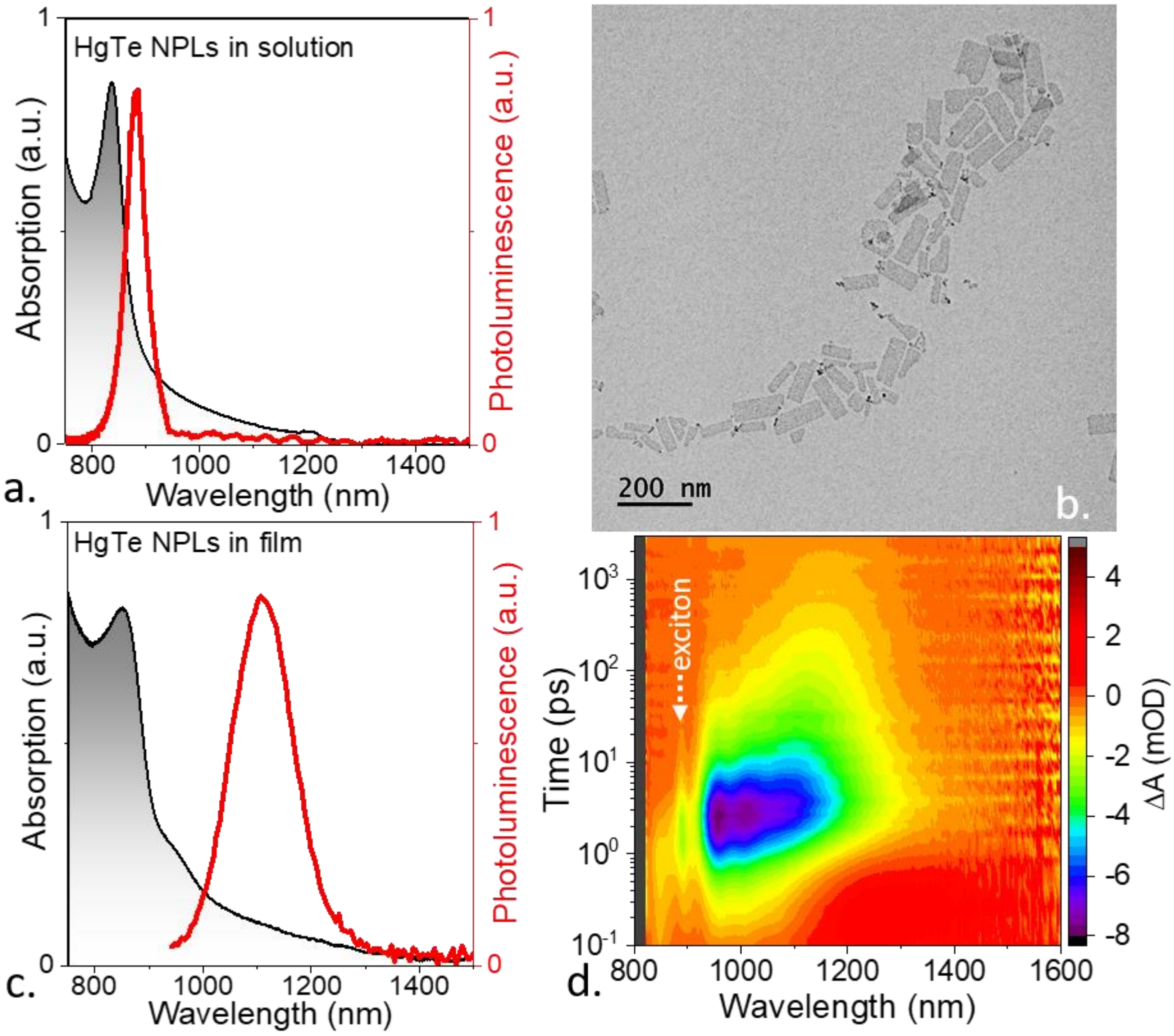

Figure 1 Spectroscopic and structural properties of HgTe NPLs*. a. Absorption and photoluminescence of fresh NPLs in solution. b. TEM image of HgTe NPLs. c. Absorption and photoluminescence of NPLs in a film. d. Transient absorption map (i.e. change of absorption spectra as a function of time) for a film excited at 350 nm. The energy of the exciton is highlighted by a white arrow.*

While fresh particles present a limited Stokes-shift (50 nm) between the absorption and the PL signals (**Figure 1**a), we observe that, in a film, the PL is strongly redshifted, see **Figure 1**c. The exact nature of this redshift remains a bit controversial since it has been attributed to the presence of parasitic HgTe quantum dots[25] or to doping[27] and trap states may also be invoked. Tenney *et al*[25] have previously observed a strong shift of the PL signal associated with a transition from the band-edge to a lower energy emissive state. However, chemical impurity doping is also reported to produce similar sub-band-gap emission[27]. To clarify this question, we have tracked the carrier dynamics using transient absorption (TA), see **Figure 1**d. Within 10 ps, the feature associated with the band edge disappears and is replaced by a broad feature that continuously shifts toward low energies at least up to the ns regime (the measurement at longer delays is limited by the delay track). Usually deep trap emission, which has a low oscillator strength, does not have a detectable TA signal, see the TA map from CdTe NPLs in Figure S2. This low energy feature is neither observed on fresh HgTe NPL (Figure S3), suggesting a non-intrinsic nature for the sub band gap feature observed on aged NPLs.

Moreover, the spectral migration on a nanosecond time-scale apparent in the data is also inconsistent with deep trap emission observed in other nanocrystal systems. In particular, transfer from the excitonic state to the traps responsible for deep trap emission is <100 ps[28], while transfer among heterogeneous nanocrystals via FRET, occurs on a timescale of ≈1 ns[29]. This last dynamic is similar to the observed spectral migration and is consistent with the work by Tenney et al[25] that proposed to connect this feature to the presence of small HgTe NCs coming as side product of the cation exchange reaction. Regarding the nature of the coupling, a first possibility would have been charge transfer in the film. In this case, the charge transfer duration will be given by $\tau_{hop} = \frac{eR^2}{6\mu k_b T}$ with e the proton charge, R the hopping length, μ the carrier mobility and k_bT the thermal energy. Since no ligand exchange is performed, the mobility is expected to be low (10^{-6} $cm^2V^{-1}s^{-1}$ with long capping ligand[30]), meaning that a 3 nm (corresponding to the thickness a NPL capped with C_{18} alkyl chain) charge transfer is expected to last 600 ns at room temperature. This time scale is much longer than the dynamics observed by TA. We can then conclude that transfer mechanism from the NPL to bound small NCs occurs through energy transfer such as FRET[31] process for which transfer duration of the order of a few ps has been reported for hybrid NPL/NC systems[32].

We additionally notice a drop of the PL magnitude under illumination, see **Figure 2**a. We attribute this to the fact that the blue light used to excite the PL can also provide enough energy to break the bonds between the ligands and the NPL surface, leaving the surface unpassivated. Inspired by works on HgTe NCs[33] and CdSe NPLs[34], we propose a modification of the surface chemistry where the initial oleylamine capping the NPLs is replaced by halides. The butylamine copassivates through hydrogen bound the monolayer of halide on the HgTe NPL surface. Besides, it can also solubilize the excess of $HgBr_2$ which could have crystallize as monolayers, due to its layered crystal structure, on top of the HgTe-Br NPLs[34,35]. By doing so, the surface chemistry of the HgTe NPLs also matches the surface chemistry of the ZnO layer that is later used as the electron transport layer in diodes. Without this ligand exchange, the deposition of ZnO on HgTe NPLs tends to quench their PL. The ligand exchange procedure can be tracked using infrared spectroscopy, see **Figure 2**b. In particular, we observe a drastic reduction of the absorbance relative to the C-H bond resonance confirming that free ligands are removed and that the ligand length is reduced (switch from C_{18} to C_4 chain). This step also enables charge conduction through the film which is essential for the design of light emitting diodes. After such treatment, the PL is more stable, see **Figure 2**c, with only a limited drop over a time scale compatible with PL measurements. A redshift is also observed, which exact magnitude may depend on the samples use (*i.e.* irradiance used to excite sample or driving bias in LED). This behavior can be associated with a partial delocalization of the wavefunctions over the halides and to out-of-plane strain induced by the ligands, which may lead to an increase of the thickness and thus a decrease of quantum confinement[36]. Such observations have already been done on colloidal suspension of CdSe and HgTe NPLs[34].

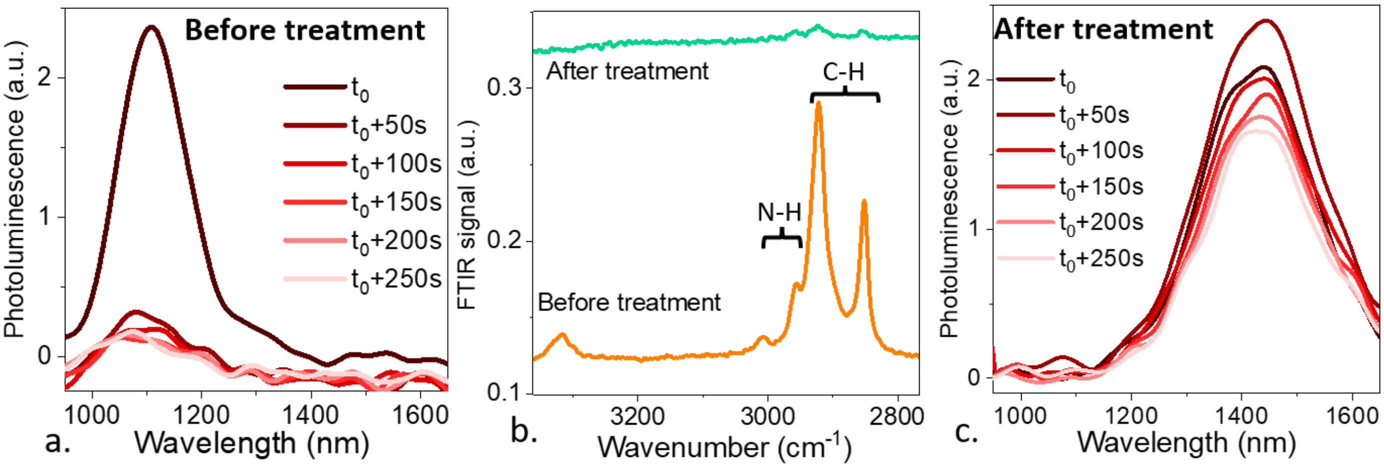

***Figure 2 Benefit of surface chemistry modification on luminescence properties**. a. PL spectra for an unprocessed HgTe NPLs film for various durations of continuous excitation by a 405 nm laser. b. Infrared absorption spectra before and after the surface chemistry modification. The curves have been shifted for the sake of clarity, but the scale is unchanged. c. PL spectra for a HgTe NPLs film after ligand exchange for various durations of continuous excitation by a 405 nm laser at low power.*

Now that we have developed a method to obtain a more stable PL from HgTe NPLs, we can consider integrating this material into photonic and optoelectronic devices. A first question that we aim to address is the demonstration of macroscopically oriented emission from an HgTe NPL array. So far most of the current strategies to demonstrate directional emission from a NPL film relies on their self-assembly[4–9] into an ensemble where they align, typically along the substrate due to their relatively large lateral extension. Here, we adopt a completely different approach, where the directionality of emission arises from the coupling to a plasmonic grating, see a schematic in **Figure 3**a. In this case, the direction of emission results from the dispersion of the plasmon[37], that can be easily tuned through the grating's geometrical factor. In this sense, our approach is closer to the one proposed by Sergeev *et al.*[38,39] using HgTe quantum dots or the one proposed for wider band gap materials.[40] We design a metallic grating made of 300 nm wide gold digits, see Figure S4. The period (*p*) of the grating is driving its optical resonance wavelength through the expression $p=\lambda/n$, where n is the film's refractive index taken equal to 2 for a HgTe NC film still capped with organic ligands[41]. To maintain PL signal, the deposition of HgTe NPLs is the final step (*i.e.* after the NPL grating get fabricated), it minimizes exposure of the active layer to non-solvent and annealing steps.

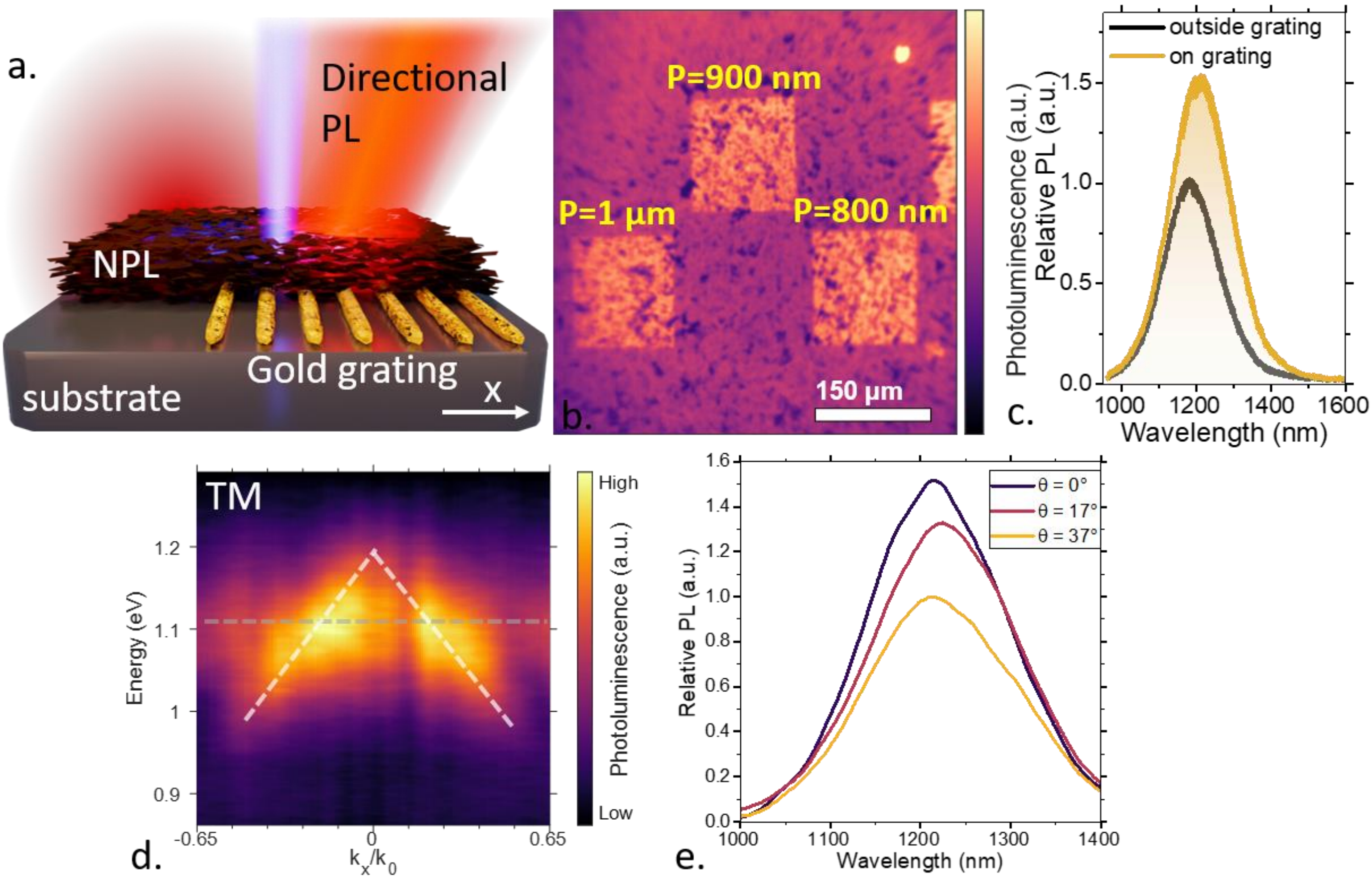

Figure 3 Luminescence from HgTe NPLs coupled to a plasmonic grating*. a. Schematic of an HgTe NPLs film deposited on a plasmonic metallic grating. b. Photoluminescence image of the HgTe film on substrate and on grating of various periods. c. Relative PL spectra outside of and on a grating (p=800 nm). d. Photoluminescence dispersion map in TM polarization (p=800 nm). e. Relative PL spectra along three directions of emission (p=800 nm). θ is defined as the angle with the normal to the sample.*

On top of the grating, the PL signal (**Figure 3**b) appears enhanced. The mechanisms at the origin of the enhancement have been previously discussed[41]. It consists of (*i*) the enhancement of the absorption at the excitation wavelength (633 nm here) through a plasmon magnified electric field and (*ii*) an increase in emission from the presence of gold that prevents the emitted light from being guided into the substrate due to the latter's large optical index. The enhancement here reaches 60 % according to the spectra measured on and away from the grating, see **Figure 3**c. In addition to the modulation of the signal's amplitude, we have also tracked the orientation of the signal by measuring the dispersion map, see **Figure 3**d and S6. The signal appears to be composed of two contributions: a non-dispersive background and some brighter tilted lines on top. We also observe that the PL signal is non dispersive on a bare substrate (Figure S5). That is, NPLs in the film do not show directional emission from anisotropic alignment. The tilted lines are then the result of the coupling to the surface plasmon's dispersion through the metallic grating, see Figure S7, while the isotropic background is attributed to NPLs that remain uncoupled due to the thickness of the film. From this dispersion map, we can extract the spectra along various directions, see **Figure 3**e. Emission occurs mostly at low angle with respect to the normal, which is the targeted configuration for efficient electroluminescence.

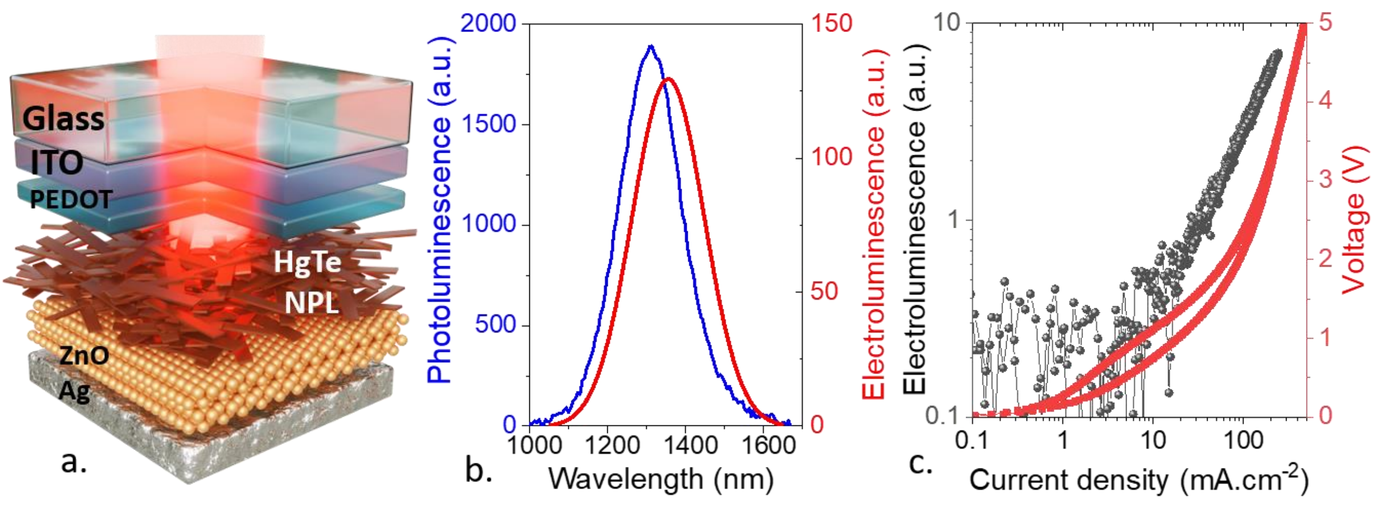

***Figure 4 Electroluminescence from HgTe NPL**. a. Schematic of the HgTe NPL-based diode. b PL and EL spectra. c. Electroluminescence and voltage as a function of the current density.*

In the last part of the paper, we explore the design of electroluminescent (EL) devices for HgTe NPLs. We use a diode stack[42] that has been proven efficient for NPL-based LEDs[43,44]. Here the hole injection is done through a PEDOT:PSS layer and the electron transport layer is made of ZnO coupled to a low work function silver electrode. Light extraction occurs on the substrate side thanks to a tin doped indium oxide (ITO) layer, see a schematic of the LED in **Figure 4**a. The EL spectrum mostly overlaps with the PL from the HgTe NPLs, as shown in **Figure 4**b. Thus, we can exclude that any other layer from the diode stack might be responsible for the EL signal. The diode presents a bias threshold at around 0.9 V which corresponds to sub-band gap operation for this material with emission at ≈1 eV, see **Figure 4**c. It is worth pointing that the LED containing unprocessed NPLs (without the above-mentioned ligand exchange procedure) do not present any EL signal, see Figure S8.

Currently the main limitation comes from the weak EL efficiency that we estimate at around 0.015%, which is two orders of magnitude lower than the value obtained with HgTe spheroid NCs.[33,45] This certainly entails to the need for core-shell heterostructures with better preservation of the PL efficiency once the NPLs are integrated within a device. Another next stage of this research will deal with the coupling of the directive emission from the grating electrode with the diode stack requested for EL, however the transfer is not straight forward since the dielectric and optical environment of the active layer is deeply modified in the diode.

To summarize, we have shown, using transient absorption, that PL from HgTe NPL films is dominated by sub band gap emissive states. However, an optimized surface chemistry modification enables a higher stability under illumination. Whereas approaches to obtain polarized and directive emission from NPL array focus on self-assembly, we propose a complementary method by coupling the film to a metallic plasmonic grating. We demonstrate a 60% increase of the PL signal as well as directional control of the emission. Finally, we demonstrated electroluminescence from this material with sub band gap operation. Future efforts will have to be focused on improving PL efficiency and stability through the synthesis of heterostructures.

METHODS

Chemicals: octadecene (ODE) (Sigma-Aldrich, 90%), cadmium acetate anhydrous ($Cd(Ac)_2$) (Sigma-Aldrich, 99.995%), cadmium oxide (CdO) (Strem 99.99%), dodecanethiol (DDT) (Sigma-Aldrich, 98%),1,2-ethanedithiol (EDT) (Fluka, 98%), mercury acetate ($Hg(Ac)_2$) (Merck, 99%), mercury chloride ($HgCl_2$) (Strem Chemicals, 99%), mercury bromide ($HgBr_2$) (Alfa Aesar), mercury iodide (HgI_2) (Touzart & Matignon), myristic acid (Sigma-Aldrich 99%), propionic acid (Sigma-Aldrich 99%), tellurium powder (Te) (Sigma-Aldrich 99.99%), oleic acid (OA), decanoic acid (Sigma-Aldrich, 98%) (Sigma-Aldrich 90%), butylamine (Alpha, 99%), oleylamine (OLA) (Acros, 80-90%), trioctylphosphine (TOP) (Alpha Aesar, 90%), tetrachloroethylene

(TCE) (VWR) toluene (VWR, 99.5%), n-hexane (VWR, 99%), ethanol (VWR, 96%). All chemicals are used as received. **Mercury compounds are highly toxic. Handle them with special care.**

1 M TOPTe precursor: 2.54 g of Te powder are mixed with 20 mL of TOP in a three-neck flask. The flask is kept under vacuum at room temperature for 5 min before the temperature was raised to 100 °C. Degassing is conducted at this temperature for 20 min. Then, the atmosphere is switched to N_2 and the temperature is raised to 275 °C. The solution is stirred until a clear orange coloration is obtained. The flask is afterwards cooled down to room temperature and the color turns to yellow. Finally, this solution is transferred to a nitrogen-filled glove box for storage.

Cadmium decanoate ($Cd(Decanoate)_2$): In a 100 mL three-neck flask, 2 g of CdO (15.7 mmol) and 6.9 g (40 mmol) of decanoic acid are mixed and heated at 210 °C for 1 h under argon atmosphere. When the entire solid is dissolved and a colorless solution is obtained, the heating is stopped and acetone is added to precipitate cadmium decanoate. The powder is centrifugated and washed at least 3 times with acetone then set under vacuum over the night.

CdTe NPL synthesis: In a 50 mL three-neck flask, 233 mg of $Cd(decanoate)_2$, 80 µL of OA and 10 mL of ODE are mixed and degassed at 90 °C for 1 h. Under argon flow, the temperature is set to 210 °C. At 185°C, 100 µL of TOPTe 1M in 500 µL of ODE is added to the mixture. When the color turns orange (after a few seconds), 70 µL of propionic acid diluted in 500 µL ODE are added. After 15 min at 210 °C, the mixture is cooled to room T. The NPLs are centrifugated twice with 15 mL of hexane and 20 mL of ethanol then redispersed in 5 mL of hexane.

Hg oleate (0.08M) ($Hg(OA)_2$): In a 50 mL three neck flask, 500 mg of $Hg(OAc)_2$ is mixed with 20 mL of OA. The mixture is heated at 80°C for 30 min. The solution is cooled down to room temperature and put under vacuum for 30 min to extract the remaining acetic acid. The solution is stored in a vial and can be used for 2-3 weeks, then metallic mercury is observed bottom of the vial.

Hg cation exchange procedure: In a glass tube, add 1 mL of CdTe (20 µmol of Cd) redispersed in 6 mL of TCE. The tubes are stored in a fridge until the temperature reaches 5°C. Then, 200 µL of $Hg(OA)_2$ (0.08 M in OA) and 400 µL of $Hg(Ac)_2$ (0.1 M in OLAm) are added. The reaction is carried out until the absorption features stabilize. The NPLs are then precipitated by adding few drops of ethanol and centrifugated at 12000 rpm for 1 min. The NPLs are finally suspended in 500 µL of toluene (final concentration of around 10 mg.mL^{-1}).

X-ray Diffraction: X-ray diffraction (XRD) sample is obtained by drop-casting the solution of nanocrystals on a Si wafer. The diffractometer is a Philips X'Pert, based on the emission of the Cu K_α (λ=0.154 nm) line operated at 40 kV and 40 mA current.

TEM: A drop of diluted NCs solution was drop-casted onto a copper grid covered with an amorphous carbon film. The grid was degassed overnight under secondary vacuum. Imaging was conducted on a Titan Themis 200 microscope (FEI/Thermo Fischer Scientific) equipped with a geometric aberration corrector on the probe. The microscope was also equipped with the "Super-X" systems for EDX analysis with a detection angle of 0.9 steradian. The observations were made at 200 kV with a probe current of about 35 pA and a half-angle of convergence of 17 mrad. HAADF-STEM images were acquired with a camera length of 110 mm (inner/outer collection angles were respectively 69 and 200 mrad).

Absorption spectroscopy: UV-visible spectra were obtained by a Cary5000 spectrometer.

Photoluminescence spectroscopy: Photoluminescence spectra on film and in solution have been collected using a Flame NIR Spectrometer equipped with an InGaAs detector from Ocean optics. The excitation has been conducted using a blue laser diode (405 nm).

Angle resolved photoluminescence measurements. Wide field photoluminescence images and dispersion relations have been obtained by pumping the samples with a tungsten filament in Köhler configuration (with a bandpass filter to select wavelengths between 400 nm and 800 nm). In other words, the sample is excited over a wide field, with a diameter approximately equal to 1 mm for the experiments with a 10X objective and 250 microns for the experiments with a 50X objective In other words, the sample is excited over a wide field, with a diameter approximately equal to 3 mm for the experiments with a 10X objective (**Figure 3**b) and 500 microns for the experiments with a 50X objective (**Figure 3**c,d an d e).We verified that the excitation power, on the order of 100-1000 W/cm^2, was low enough to have à PL signal in the unsaturated regime. To obtain photoluminescent images, the PL signal is separated from the optical pump with a dichroic mirror and a long-pass colored glass filter and sent to a NIRvana 640ST InGaAs camera from Princeton Instruments via a Telan lens and an SP2356 Acton spectrometer (also from Princeton Instruments) in imaging mode. To obtain dispersion relations, the Acton spectrometer is used in monochromator mode and a Bertrand lens is added in the optical path to image the reciprocal space (*i.e.* the back focal plane of the objective).

FTIR spectroscopy: Infrared spectroscopy is conducted using a Vertex 70 Michelson interferometer from Bruker. The instrument is coupled to an attenuated total reflection setup. The beam splitter is made of XT-Br crystal and the detection is made using a DTGS (Deuterated Triglycine Sulfate) detector.

Transient absorption Measurements were performed by splitting the 800 nm fundamental of a 5 kHz, 60 fs Ti: sapphire laser into pump and probe branches. The pump branch was directed through an OPA to generate 700 nm pump pulses and chopped to 2.5 kHz; the probe branch was optically delayed using a variable delay stage with retroreflector and then focused into a 5 mm thick sapphire plate to generate a supercontinuum in the near-infrared. The pump and probe pulses were spatially-overlapped at the sample position and spectra were collected by differencing pump-on and pump-off spectra.

Grating fabrication: In a cleanroom, Si/SiO_2 substrates (400 nm oxide layer) are thoroughly washed by first spraying them with acetone then sonicating them in an acetone bath for 5 min. Acetone is sprayed a second time followed by IPA, which is dried with N_2. The substrates are then put into an O_2 plasma cleaner for 7 minutes at 30 W. Once the substrates are cleaned, PMMA is deposited on top to prepare them for E-beam lithography. Roughly 300 nm of PMMA are deposited by spin-coating a pre-prepared solution of PMMA in anisole at 4000 rpm for 30s, followed by 3 minutes of annealing at 175°C on a heating plate. Thus prepared, the substrates are put into a Zeiss Supra 40 SEM with Raith ELPHYS Quantum device and e-beam lithography is performed according to the grating design. The operating bias is set to 20 kV, the aperture to 10 µm, and the dose to 160 µC/cm² The PMMA is then developed in an MIBK:IPA solution (1:3) for 60s, then washed with IPA and dried with N_2. The developed substrates are cleaned in an O_2 plasma cleaner for 3 minutes at 30 W. Using a VINCI thermal evaporator, 5 nm of Ti followed by 50 nm of Au are deposited. The PMMA is lifted-off by putting the substrates in acetone for 1 day. Once cleaned a last time for 3 minutes in an O_2 plasma cleaner at 30 W, the substrates are ready for film deposition.

Input for electromagnetic simulation: For the air and Si substrate, the real parts of the refractive indices are set to 1 and 3.5, respectively, and the imaginary parts are both set to 0. For the natural SiO_2 layer, refractive index is set to 1.5. For gold, the dielectric function from Drude model $\varepsilon(E) = 1 - 2.29 \times 10^7 / [E(E+i130)]$, with E the photon energy in meV, is used. For the NPL film, we set the refractive index equal to 1.65, while the spectral dependence of the imaginary part of the optical index is taken from the film absorption spectrum (**Figure 1**c), while matching the exciton feature at 0.1.

Simulations: Optical properties of the structure are simulated with COMSOL Multiphysics, *2D Frequency Domain Interface using RF module*. Periodicity is set for boundary conditions at the side edges. A periodic port to generate incoming electromagnetic wave is placed above the structure (*i.e.,* in the region defined as air). Above the air and below the Si substrate, two perfectly matched layers are added to absorb outgoing waves and minimize possible nonphysical reflections due to limited size. Physical-controlled mesh is enabled with extremely fine element size. The dissipated power per unit volume in the metals and nanocrystals can be calculated using the formula $P = -0.5\omega|F|^2 Im(\varepsilon)$, where F is the electric field, ω is the angular frequency of the incident wave, and $Im(\varepsilon)$ is the imaginary part of the material permittivity. The absorption within a material is calculated by integrating the dissipated power over the volume of the material, then dividing it by the incident power defined in the port.

Materials for LED: PEDOT:PSS (poly(3,4-ethylenedioxythiophene) polystyrene sulfonate, Al 4083, M121, Ossila), , PMMA (polymethyl metacrylate, Arkema), , epoxy-glue (Ossila), zinc acetate dihydrate (<97%, Alfa Aesar), tetramethylammonium hydroxide pentahydrate (TMAOH, 98%, Alfa Aesar), dimethyl sulfoxide (DMSO, ≥99.9%, Sigma-Aldrich), ethyl acetate (VMR), ethanol absolute anhydrous (VMR), octane (VWR, technical), toluene (VWR 99.5%) and acetone (VWR). All the materials were used as received.

Synthesis of ZnO nanoparticles: The procedure is taken from ref [42]. In flask A, 3 mmol of zinc acetate are dissolved in 30 mL of DMSO by vigorous stirring. At the same time, 5.5 mmol of TMAOH are dissolved with 10 mL of ethanol in flask B. Then the contents of the two flasks are mixed and stirred for 24 hours under ambient conditions. The reaction mixture turns whitish during the first few seconds and becomes clear soon after. ZnO particles are precipitated by ethyl acetate and redisperse in ethanol. 160 µL of 2-ethanolamine are added to stabilize the nanoparticles before they are precipitated and redispersed with ethyl acetate and ethanol respectively again. Finally, the ZnO nanoparticles in ethanol are filtered using a 0.22 µm PTFE filter.

ITO substrate patterning: ITO substrates (30 Ω/sq) are cut into 15 mm × 15 mm pieces and cleaned by sonication in acetone for 5 min. After sonication, the substrates are rinsed with acetone and isopropanol before being dried completely with N_2 flow. The substrates are further cleaned with O_2 plasma for 5 min to remove organic residuals on the surface. After cleaning, TI-Prime and AZ 5214E photoresist are sequentially spin-coated on the surface of ITO substrates at the rate of 4000 rpm for 30 s and baked at 110 °C for 120 s and 90 s, respectively. In the next stage, a mask aligner is used to expose the substrates to UV light for 20 s through a lithography mask (1 mm width). A photoresist is then developed using AZ 726 developer for 20 s before rinsing with deionized water and drying with N_2 flux. After another 5-minutes plasma cleaning, the substrates are etched in a 25% HCl (in water) bath for 10 min at 40 °C before they are dipped immediately in deionized water. Finally, the lift-off is conducted in an acetone bath. Before being used, the patterned ITO substrates are cleaned with acetone and isopropanol first and put under plasma for 10 min.

LED Fabrication: PEDOT:PSS solution (filtered through 0.45 µm filter) is spin-coated on a patterned ITO glass electrode at 4000 rpm for 60 s and annealed at 140 °C for 10 min in air. NPLs (in toluene (10 mg.mL^{-1})) are spin-coated at 2000 rpm for 45s. The obtained film is swiftly dipped in a solution of solution of $HgBr_2$ (0.1 M in methanol) for 5 min and dried before a second dipping of 15 s inside a solution of butylamine in methanol (10%) for 15s. Three successive NPLs deposition and ligand exchange are carried out before depositing ZnO nanoparticles by spin-coating at 2000 rpm for 45 s. Finally, 80 nm of Ag is deposited on top of the ZnO using a shadow mask by thermal evaporation. The thickness of NPL and ZnO layers are around 300 nm and 70 nm respectively, as obtained by profilometry. The devices are encapsulated inside the glove box with a piece of glass by epoxy-glue. The size of the pixel is 1 mm^2 which is the overlap of ITO and Ag electrodes.

LED characterization: EL spectra are collected by a Flame NIR Spectrometer equipped with an InGaAs detector from Ocean optics while passing a constant current with a Keithley 2400. The EQE of the device is determined according to the method from Ref [46]. For the characterization, we collected current-voltage-radiance characteristics with a Keithley K2400B sourcemeter unit and a PM100A powermeter coupled with the S122C Ge detector from Thorlabs. Considering the Lambertian emission of the LED device, the flux leaving the device in the direction of the detector can be described as $F_{\mathrm{ext}} = \int_0^{\pi/2} 2\pi L_0 \cos\theta \sin\theta d\theta = \pi L_0$, with $L_0 cos\theta$ the flux per solid angle of light leaving the device in the forward direction. Since the solid angle from the photodetector to the light source is $\Omega = \frac{S_1}{l^2} \approx 1.7$ with S_1 the area of the detector and l the distance between the light source and detector, then $L_0 = \frac{P_{\mathrm{det}}}{\Omega} = \frac{P_{\mathrm{det}} l^2}{s_1}$ and $F_{\mathrm{ext}} = \frac{\pi P_{\mathrm{det}} l^2}{s_1}$, with P_{det} the optical power measured by the detector. The number of photons emitted per second to the forward direction can then be calculated by $N_P = \frac{F_{\mathrm{ext}}}{h\nu} = \frac{\pi P_{\mathrm{det}} l^2 \lambda}{s_1 hc}$, with λ the wavelength of electroluminescence, h the Planck's constant and c the speed of light. The number of electrons injected per second can be obtained by $N_P = \frac{I}{e}$, with I the current flowing in the device. Thus, the EQE can be calculated as EQE $= \frac{N_p}{N_e} = \frac{\pi P_{det} l^2 \lambda e}{s_1 hcI}$. The irradiance of the device is $R = \frac{F_{\text{ext}}}{s_2} = \frac{\pi P_{\text{det}} l^2}{s_1 s_2}$, with S_2 the area of the pixel (1mm²).

SUPPORTING INFORMATION

Supporting Information include details about (*i*) material properties of CdTe NPLs and impact of the halide treatment. (*ii*) Experimental and modelling of the dispersion of the HgTe NPL film and (*iii*) additional measurement relative to electroluminescence.

ACKNOWLEDGEMENTS

The project is supported by ERC grants blackQD (grant n° 756225), Ne2deM (grant 853049), FORWARD (grant n° 771688) and AQDtive (grant n°101086358). This work was supported by French state funds managed by the Agence Nationale de la recherche (ANR) through the grant IPER-Nano2 (ANR-18CE30-0023-01), Copin (ANR-19-CE24-0022), Frontal (ANR-19-CE09-0017), Graskop (ANR-19-CE09-0026), NITQuantum (ANR-20-ASTR-0008), Bright (ANR-21-CE24-0012), MixDFerro (ANR-21-CE09-0029) and Quicktera (ANR-22-CE09-0018). Work performed at the Center for Nanoscale Materials, a U.S. Department of Energy Office of Science User Facility, was supported by the U.S. DOE, Office of Basic Energy Sciences, under Contract No. DE-AC02-06CH11357. This work was done within the C2N micro nanotechnologies platforms and partly supported by the RENATECH network.

CONFLICT OF INTEREST

The authors declare no competing financial interest.

REFERENCES

(1) Erdem, T.; Demir, H. V. Color Science of Nanocrystal Quantum Dots for Lighting and Displays. *Nanophotonics* **2013**, *2*, 57–81.

(2) Dabard, C.; Guilloux, V.; Gréboval, C.; Po, H.; Makke, L.; Fu, N.; Xu, X. Z.; Silly, M. G.; Patriarche, G.; Lhuillier, E.; Barisien, T.; Climente, J. I.; Diroll, B. T.; Ithurria, S. Double-Crowned 2D Semiconductor Nanoplatelets with Bicolor Power-Tunable Emission. *Nat. Commun.* **2022**, *13*, 5094.

(3) Diroll, B. T.; Guzelturk, B.; Po, H.; Dabard, C.; Fu, N.; Makke, L.; Lhuillier, E.; Ithurria, S. 2D II–VI Semiconductor Nanoplatelets: From Material Synthesis to Optoelectronic Integration. *Chem. Rev.* **2023**, *123*, 3543-3624.

(4) Momper, R.; Zhang, H.; Chen, S.; Halim, H.; Johannes, E.; Yordanov, S.; Braga, D.; Blülle, B.; Doblas, D.; Kraus, T.; Bonn, M.; Wang, H. I.; Riedinger, A. Kinetic Control over Self-Assembly of Semiconductor Nanoplatelets. *Nano Lett.* **2020**, *20*, 4102–4110.

(5) Gao, Y.; Weidman, M. C.; Tisdale, W. A. CdSe Nanoplatelet Films with Controlled Orientation of Their Transition Dipole Moment. *Nano Lett.* **2017**, *17*, 3837–3843.

(6) Bai, P.; Hu, A.; Liu, Y.; Jin, Y.; Gao, Y. Printing and *In Situ* Assembly of CdSe/CdS Nanoplatelets as Uniform Films with Unity In-Plane Transition Dipole Moment. *J. Phys. Chem. Lett.* **2020**, *11*, 4524–4529.

(7) Baruj, H. D.; Bozkaya, I.; Canimkurbey, B.; Isik, A. T.; Shabani, F.; Delikanli, S.; Shendre, S.; Erdem, O.; Isik, F.; Demir, H. V. Highly-Directional, Highly-Efficient Solution-Processed Light-Emitting Diodes of All-Face-Down Oriented Colloidal Quantum Well Self-Assembly. *Small* **2023***,* 2206582.

(8) Kim, W. D.; Kim, D.; Yoon, D.-E.; Lee, H.; Lim, J.; Bae, W. K.; Lee, D. C. Pushing the Efficiency Envelope for Semiconductor Nanocrystal-Based Electroluminescence Devices Using Anisotropic Nanocrystals. *Chem. Mater.* **2019**, *31*, 3066–3082.

(9) Lee, K. J.; Bera, R.; Kang, J.; Jeong, K. S.; Cho, M. Orientation-Dependent Image Dipole Interaction for the Tuning of the Excitonic Properties of CdSe Nanoplatelets. *J. Phys. Chem. C* **2023**, *127*, 1937–1943.

(10) Abécassis, B.; Tessier, M. D.; Davidson, P.; Dubertret, B. Self-Assembly of CdSe Nanoplatelets into Giant Micrometer-Scale Needles Emitting Polarized Light. *Nano Lett.* **2014**, *14*, 710–715.

(11) Cunningham, P. D.; Souza, J. B.; Fedin, I.; She, C.; Lee, B.; Talapin, D. V. Assessment of Anisotropic Semiconductor Nanorod and Nanoplatelet Heterostructures with Polarized Emission for Liquid Crystal Display Technology. *ACS Nano* **2016**, *10*, 5769–5781.

(12) Beaudoin, E.; Abecassis, B.; Constantin, D.; Degrouard, J.; Davidson, P. Strain-Controlled Fluorescence Polarization in a CdSe Nanoplatelet–Block Copolymer Composite. *Chem. Commun.* **2015**, *51*, 4051–4054.

(13) Gréboval, C.; Izquierdo, E.; Livache, C.; Martinez, B.; Dufour, M.; Goubet, N.; Moghaddam, N.; Qu, J.; Chu, A.; Ramade, J.; Aubin, H.; Cruguel, H.; Silly, M.; Lhuillier, E.; Ithurria, S. Impact of Dimensionality and Confinement on the Electronic Properties of Mercury Chalcogenide Nanocrystals. *Nanoscale* **2019**, *11*, 3905–3915.

(14) Galle, T.; Samadi Khoshkhoo, M.; Martin-Garcia, B.; Meerbach, C.; Sayevich, V.; Koitzsch, A.; Lesnyak, V.; Eychmüller, A. Colloidal PbSe Nanoplatelets of Varied Thickness with Tunable Optical Properties. *Chem. Mater.* **2019**, *31*, 3803–3811.

(15) Biesterfeld, L.; Klepzig, L. F.; Niebur, A.; Rosebrock, M.; Lauth, J. Toward Bright Colloidal Near-Infrared Emitters: Surface Passivation of 2D PbSe Nanoplatelets by Metal Halides. *J. Phys. Chem. C* **2022**, *126*, 19277–19285.

(16) Salzmann, B. B. V.; Wit, J. de; Li, C.; Arenas-Esteban, D.; Bals, S.; Meijerink, A.; Vanmaekelbergh, D. Two-Dimensional CdSe-PbSe Heterostructures and PbSe Nanoplatelets: Formation, Atomic Structure, and Optical Properties. *J. Phys. Chem. C* **2022**, *126*, 1513–1522.

(17) Moghaddam, N.; Gréboval, C.; Qu, J.; Chu, A.; Rastogi, P.; Livache, C.; Khalili, A.; Xu, X. Z.; Baptiste, B.; Klotz, S.; Fishman, G.; Capitani, F.; Ithurria, S.; Sauvage, S.; Lhuillier, E. The Strong Confinement Regime in HgTe Two-Dimensional Nanoplatelets. *J. Phys. Chem. C* **2020**, *124*, 23460–23468.

(18) Izquierdo, E.; Dufour, M.; Chu, A.; Livache, C.; Martinez, B.; Amelot, D.; Patriarche, G.; Lequeux, N.; Lhuillier, E.; Ithurria, S. Coupled HgSe Colloidal Quantum Wells through a Tunable Barrier: A Strategy To Uncouple Optical and Transport Band Gap. *Chem. Mater.* **2018**, *30*, 4065–4072.

(19) Livache, C.; Izquierdo, E.; Martinez, B.; Dufour, M.; Pierucci, D.; Keuleyan, S.; Cruguel, H.; Becerra, L.; Fave, J. L.; Aubin, H.; Ouerghi, A.; Lacaze, E.; Silly, M. G.; Dubertret, B.; Ithurria, S.; Lhuillier, E. Charge Dynamics and Optolectronic Properties in HgTe Colloidal Quantum Wells. *Nano Lett.* **2017**, *17*, 4067–4074.

(20) Mitrofanov, A.; Prudnikau, A.; Di Stasio, F.; Weiß, N.; Hübner, R.; Dominic, A. M.; Borchert, K. B. L.; Lesnyak, V.; Eychmüller, A. Near-Infrared-Emitting CdxHg1–XSe-Based Core/Shell Nanoplatelets. *Chem. Mater.* **2021**, *33*, 7693–7702.

(21) Schliehe, C.; Juarez, B. H.; Pelletier, M.; Jander, S.; Greshnykh, D.; Nagel, M.; Meyer, A.; Foerster, S.; Kornowski, A.; Klinke, C.; Weller, H. Ultrathin PbS Sheets by Two-Dimensional Oriented Attachment. *Science* **2010**, *329*, 550–553.

(22) Gréboval, C.; Chu, A.; Goubet, N.; Livache, C.; Ithurria, S.; Lhuillier, E. Mercury Chalcogenide Quantum Dots: Material Perspective for Device Integration. *Chem. Rev.* **2021**, *121*, 3627–

(23) Izquierdo, E.; Robin, A.; Keuleyan, S.; Lequeux, N.; Lhuillier, E.; Ithurria, S. Strongly Confined HgTe 2D Nanoplatelets as Narrow Near-Infrared Emitters. *J. Am. Chem. Soc.* **2016**, *138*, 10496–10501.

(24) Dabard, C.; Planelles, J.; Po, H.; Izquierdo, E.; Makke, L.; Gréboval, C.; Moghaddam, N.; Khalili, A.; Dang, T. H.; Chu, A.; Pierini, S.; Abadie, C.; Cavallo, M.; Bossavit, E.; Xu, X. Z.; Hollander, P.; Silly, M.; Lhuillier, E.; Climente, J. I.; Ithurria, S. Optimized Cation Exchange for Mercury Chalcogenide 2D Nanoplatelets and Its Application for Alloys. *Chem. Mater.* **2021**, *33*, 9252–9261.

(25) Tenney, S. M.; Vilchez, V.; Sonnleitner, M. L.; Huang, C.; Friedman, H. C.; Shin, A. J.; Atallah, T. L.; Deshmukh, A. P.; Ithurria, S.; Caram, J. R. Mercury Chalcogenide Nanoplatelet–Quantum

Dot Heterostructures as a New Class of Continuously Tunable Bright Shortwave Infrared Emitters. *J. Phys. Chem. Lett.* **2020**, *11*, 3473–3480.

(26) Anand, A.; Zaffalon, M. L.; Cova, F.; Pinchetti, V.; Khan, A. H.; Carulli, F.; Brescia, R.; Meinardi, F.; Moreels, I.; Brovelli, S. Optical and Scintillation Properties of Record-Efficiency CdTe Nanoplatelets toward Radiation Detection Applications. *Nano Lett.* **2022**, *22*, 8900-8907.

(27) Sokolova, A. V.; Skurlov, I. D.; Babaev, A. A.; Perfenov, P. S.; Miropoltsev, M. A.; Danilov, D. V.; Baranov, M. A.; Kolesnikov, I. E.; Koroleva, A. V.; Zhizhin, E. V.; Litvin, A. P.; Fedorov, A. V.; Cherevkov, S. A. Near-Infrared Emission of HgTe Nanoplatelets Tuned by Pb-Doping. *Nanomaterials* **2022**, *12*, 4198.

(28) Baker, D. R.; Kamat, P. V. Tuning the Emission of CdSe Quantum Dots by Controlled Trap Enhancement. *Langmuir* **2010**, *26*, 11272–11276.

(29) Poulikakos, L. V.; Prins, F.; Tisdale, W. A. Transition from Thermodynamic to Kinetic-Limited Excitonic Energy Migration in Colloidal Quantum Dot Solids. *J. Phys. Chem. C* **2014**, *118*, 7894–7900.

(30) Liu, Y.; Gibbs, M.; Puthussery, J.; Gaik, S.; Ihly, R.; Hillhouse, H. W.; Law, M. Dependence of Carrier Mobility on Nanocrystal Size and Ligand Length in PbSe Nanocrystal Solids. *Nano Lett.* **2010**, *10*, 1960–1969.

(31) Hildebrandt, N.; Spillmann, C. M.; Algar, W. R.; Pons, T.; Stewart, M. H.; Oh, E.; Susumu, K.; Díaz, S. A.; Delehanty, J. B.; Medintz, I. L. Energy Transfer with Semiconductor Quantum Dot Bioconjugates: A Versatile Platform for Biosensing, Energy Harvesting, and Other Developing Applications. *Chem. Rev.* **2017**, *117*, 536–711.

(32) Williams, K. R.; Diroll, B. T.; Watkins, N. E.; Rui, X.; Brumberg, A.; Klie, R. F.; Schaller, R. D. Synthesis of Type I PbSe/CdSe Dot-on-Plate Heterostructures with Near-Infrared Emission. *J. Am. Chem. Soc.* **2019**, *141*, 5092–5096.

(33) Bossavit, E.; Qu, J.; Abadie, C.; Dabard, C.; Dang, T.; Izquierdo, E.; Khalili, A.; Gréboval, C.; Chu, A.; Pierini, S.; Cavallo, M.; Prado, Y.; Parahyba, V.; Xu, X. Z.; Decamps-Mandine, A.; Silly, M.; Ithurria, S.; Lhuillier, E. Optimized Infrared LED and Its Use in an All-HgTe Nanocrystal-Based Active Imaging Setup. *Adv. Opt. Mater.* **2022**, *10*, 2101755.

(34) Dufour, M.; Qu, J.; Greboval, C.; Méthivier, C.; Lhuillier, E.; Ithurria, S. Halide Ligands To Release Strain in Cadmium Chalcogenide Nanoplatelets and Achieve High Brightness. *ACS Nano* **2019**, *13*, 5326–5334.

(35) Yao, Y.; Zhou, Y.; Sanderson, W. M.; Loomis, R. A.; Buhro, W. E. Metal-Halide-Ligated Cadmium Selenide Quantum Belts by Facile Surface Exchange. *Chem. Mater.* **2018**, *30*, 2848–2857.

(36) Greenwood, A. R.; Mazzotti, S.; Norris, D. J.; Galli, G. Determining the Structure–Property Relationships of Quasi-Two-Dimensional Semiconductor Nanoplatelets. *J. Phys. Chem. C* **2021**, *125*, 4820–4827.

(37) Azizov, R.; Sinev, I.; Işık, F.; Shabani, F.; Pushkarev, A.; Yurdakul, I.; Delikanli, S.; Demir, H. V.; Makarov, S. Direct Laser Writing of Resonant Periodic Nanostructures in Thin Light-Emitting Films of CdSe/CdZnS Core/Shell Nanoplatelets. *Appl. Phys. Lett.* **2022**, *121*, 223301.

(38) Sergeev, A. A.; Pavlov, D. V.; Kuchmizhak, A. A.; Lapine, M. V.; Yiu, W. K.; Dong, Y.; Ke, N.; Juodkazis, S.; Zhao, N.; Kershaw, S. V.; Rogach, A. L. Tailoring Spontaneous Infrared Emission of HgTe Quantum Dots with Laser-Printed Plasmonic Arrays. *Light Sci. Appl.* **2020**, *9*, 16.

(39) Sergeev, A. A.; Sergeeva, K. A.; Pavlov, D. V.; Kuchmizhak, A. A. Enhancement of Infrared-Emitting Quantum Dots Photoluminescence Via Plasmonic Nanoarrays. *Bull. Russ. Acad. Sci. Phys.* **2022**, *86*, S196–S200.

(40) Guo, R.; Derom, S.; Väkeväinen, A. I.; van Dijk-Moes, R. J. A.; Liljeroth, P.; Vanmaekelbergh, D.; Törmä, P. Controlling Quantum Dot Emission by Plasmonic Nanoarrays. *Opt. Express* **2015**, *23*, 28206.

(41) Bossavit, E.; Dang, T.H.; He, P.; Cavallo, M.; Khalili, A.; Dabard, C.; Zhang, H.; Gacemi, D.; Silly, M. G.; Abadie, C.; Pierucci, D.; Todorov, Y.; Sirtori, C.; Diroll, B.T.; Degiron, A.; Lhuillier, E.; Vasanelli, A. Plasmon-assisted directional infrared photoluminescence of HgTe nanocrystals, *submitted* **2023**

(42) Dai, X.; Zhang, Z.; Jin, Y.; Niu, Y.; Cao, H.; Liang, X.; Chen, L.; Wang, J.; Peng, X. Solution-Processed, High-Performance Light-Emitting Diodes Based on Quantum Dots. *Nature* **2014**, *515*, 96–99.

(43) Qu, J.; Rastogi, P.; Gréboval, C.; Livache, C.; Dufour, M.; Chu, A.; Chee, S.-S.; Ramade, J.; Xu, X. Z.; Ithurria, S.; Lhuillier, E. Nanoplatelet-Based Light-Emitting Diode and Its Use in All-Nanocrystal LiFi-like Communication. *ACS Appl. Mater. Interfaces* **2020**, *12*, 22058–22065.

(44) Zhang, H.; Guilloux, V.; Bossavit, E.; Fu, N.; Dabard, C.; Cavallo, M.; Dang, T. H.; Khalili, A.; Abadie, C.; Alchaar, R.; Gréboval, C.; Xu, X. Z.; Utterback, J. K.; Pierucci, D.; Ithurria, S.; Climente, J. I.; Barisien, T.; Lhuillier, E. Visible and Infrared Nanocrystal-Based Light Modulator with CMOS Compatible Bias Operation. *ACS Photonics* **2023**, *10*, 430–436.

(45) Qu, J.; Rastogi, P.; Gréboval, C.; Lagarde, D.; Chu, A.; Dabard, C.; Khalili, A.; Cruguel, H.; Robert, C.; Xu, X. Z.; Ithurria, S.; Silly, M. G.; Ferré, S.; Marie, X.; Lhuillier, E. Electroluminescence from HgTe Nanocrystals and Its Use for Active Imaging. *Nano Lett.* **2020**, *20*, 6185–6190.

(46) Chen, Z.-Q.; Ding, F.; Bian, Z.-Q.; Huang, C.-H. Efficient Near-Infrared Organic Light-Emitting Diodes Based on Multimetallic Assemblies of Lanthanides and Iridium Complexes. *Org. Electron.* **2010**, *11*, 369–376.